Reliable underwater dipole source characterization in 3D space by an optimally designed artificial lateral line system

2017 Bioinspir. Biomim. 12 036010

(http://iopscience.iop.org/1748-3190/12/3/036010)

Bioinspiration & Biomimetics

PAPER

Reliable underwater dipole source characterization in 3D space by an optimally designed artificial lateral line system

RECEIVED
9 October 2016

REVISED
14 March 2017

ACCEPTED FOR PUBLICATION
28 March 2017

PUBLISHED
19 April 2017

Ali Ahrari[1], Hong Lei[2], Montassar Aidi Sharif[2], Kalyanmoy Deb[2] and Xiaobo Tan[2]

[1] Department of Mechanical Engineering, Michigan State University, East Lansing, MI, United States of America
[2] Department of Electrical and Computer Engineering, Michigan State University, East Lansing, MI, United States of America

E-mail: aliahrari1983@gmail.com

Keywords: inverse problem, bi-level optimization, uncertain environment, dipole source characterization, optimal design

Abstract

Inspired by the lateral line of aquatic vertebrates, an artificial lateral line (ALL) system can localize and track an underwater moving object by analyzing the ambient flow caused by its motion. There are several studies on object detection, localization and tracking by ALL systems, but only a few have investigated the optimal design of the ALL system, the one that on average provides the highest characterization accuracy. Design optimization is particularly important because the uncertainties in the employed flow model and in sensor measurements deteriorate the reliability of sensing. This study investigates the optimal design of the ALL system in three-dimensional (3D) space for dipole source characterization. It highlights some challenges specific to the 3D setting and demonstrates the shortcomings of the designs in which all sensors and their sensing directions are in the same plane. As an alternative, it proposes two design concepts, called 'Offset Strategy' and 'Angle Strategy' to overcome these shortcomings. It investigates potentials of having a swarm of cooperative ALLs as well. It performs design optimization in the presence of sensor and model uncertainties and analyzes the trade-off between the number of sensors and characterization accuracy. The obtained solutions are analyzed to reveal their strategies in solving the problem efficiently. The dependency of the optimized solutions on the uncertainties is also demonstrated.

1. Introduction

The lateral line system of fish, comprised of arrays of mechanoreceptive units called neuromasts, is an important organ sensitive to fluid motion around the fish's body [1]. It is involved in various biological behaviors [2], such as schooling [3], station holding [4], rheotaxis [5], predator sensing [6], and objects detection [7]. There are two types of neuromasts, superficial neuromasts and canal neuromasts. The superficial neuromasts are located externally on the fish skin and respond to flow velocities [8]. The canal neuromasts can be found in fluid-filled canals below the skin surface, responding to flow accelerations [8]. The interactions between the flow and the neuromasts generate neuronal pulses which are transmitted to the central nervous system for further information processing [9].

The biological lateral line has inspired several efforts in developing an engineering equivalent of analogous sensing modality for underwater applications. Over the last decade, microfabricated flow sensors, motivated by fish neuromasts, have been developed at micro-to-millimeter scales, which are based on hot wire anemometry (HWA) [10, 11], strain gauge [12], pressure sensor [13], and novel sensing materials such as ionic polymer-metal composites (IPMCs) [14]. An artificial lateral line (ALL) system (figure 1) can function as a novel sensing modality generating no noise to the environment [15], and assist underwater robots and vehicles for the navigation and control when traditional underwater sensing strategies such as vision or sonar are inhibited.

There has been some theoretical work on flow modeling and information processing to extract information from ALLs [16–21]. Some studies have demonstrated the correlation between the biological lateral line layout and the hydrodynamic pressure distribution on moving fish [22], and the influence of fish self-motion on lateral line sensing [23], which give some insights into the configuration of distributed pressure sensors of an ALL system. Most previous studies focused on the localization of a vibrating sphere, i.e. the dipole source [24–26], which emulates tail movements of fish or flickering of insects in water.

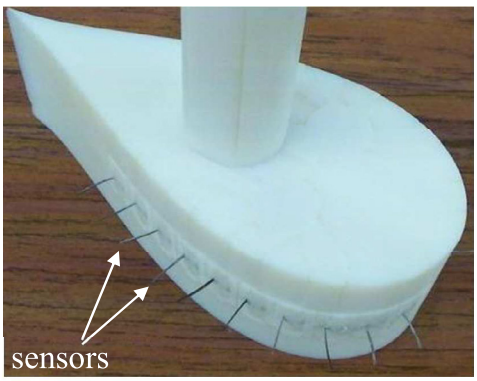

Figure 1. A prototype of an artificial lateral line system (streamlined body + flow sensing sensors).

Some other studies aimed at tracking moving objects or vortices [27–30], where arrays of commercial pressure sensors were typically adopted.

Most of the aforementioned studies adapted fixed designs following engineering intuition or biological observations. In the simplest and the most common case, the ALL consists of one or two sets of aligned sensors with uniform spacing [24, 28–31]. The diversity of information gained by such an arrangement of sensors could be limited. A cylindrical ALL body with two perpendicular arrays of sensors, as used in [32], can provide more diverse information from the sensors. Sensor arrangement mimicking biological inspiration may justify the design employed in [27], in which 16 sensors were scattered in 3D space around the nose, which was inspired by the goldfish lateral line. The advantages of such 3D arrangement over 2D arrangement was demonstrated for unsteady flow characterization. Nevertheless, there is no analytical evidence that this is the best arrangement, especially considering that the optimal design depends on the number of sensors and the amount of uncertainties in sensing and in the employed model [33]. Here by optimal design, we mean a design that provides the maximal average characterization accuracy when all possible dipole sources with different locations, vibration amplitudes and orientations are considered

Despite numerous studies on dipole detection or localization using an ALL system, very few have concentrated on finding the optimal ALL system. DeVries and Paley [18] optimized the placement of flow sensors based on the observability for the control purpose. The proposed estimation and optimization were performed in a uniform flow field. The adopted flow model was assumed to be accurate, while like most other analytically derived models, it relies on assumptions such as inviscid laminar flow and absence of walls or interfering objects that may be violated in real situations. In [26], micro-fabricated flow-sensor arrays were used to reconstruct the velocity field generated by a dipole source. Navier–Stokes equation was used to characterize the dipole-field which was limited to two dimensions. Since the hair sensors were microfabricated on a substrate, no modeling on the sensing platform or optimal configuration of sensor units have been discussed. In another study [24], a simple configuration of an ALL in which the distance between six equally spaced sensors was optimized to maximize localization accuracy for a predefined set of dipoles. Sensing directions and locations of the sensors were aligned the horizontal direction. The simple arrangement of sensors and limited number of decision parameters (one in this case) limits the characterization accuracy, even for the optimized design. At the same time, using a fixed set of sample dipoles cannot represent the general case and may result in specialized optimal designs, the designs that may characterize only that specific set of dipoles reliably.

More recent studies [25, 33] have overcome the specialization risk by random selection of sample dipoles. The parameters of the ALL system, including the shape and the size of the streamlined body, and the number and locations of in-plane flow velocity sensors were optimized such that the average accuracy of characterization was maximized while two types of uncertainties were considered in the problem. The main shortcoming of these studies is that they assumed a 2D problem setting, where the dipoles lie and vibrate only in the ALL plane. As we will demonstrate, the findings from 2D setting cannot directly be generalized to the 3D setting, a more realistic scenario in which dipole locations or vibration orientation might be out of the plane of the ALL body.

The present study, based on a streamlined body with z-axis protrusion, extends this method for dipole source characterization in the 3D space. The choice of a streamlined body is motivated by several factors, including the convenience in parameterizing its shape and size, the capacity for accommodating variation of sensor orientation and z-axis offset, and, to some extent, the resemblance to the shape of some aquatic robots (robotic boats or robotic fish), for which an ALL might be useful. We demonstrate that the design model employed in the previous studies results in blind regions: A dipole located in these regions cannot be correctly characterized by an ALL. Some alternatives are proposed to address this problem, which are tested subsequently.

The rest of this article is organized as follows: section 2 reviews the dipole characterization problem and formulates the design optimization problem. Section 3 identifies some shortcomings in conventional designs of an All. Alternatives are also proposed and tested. Optimized deigns are presented in section 4 and the tradeoff between the number of sensors and accuracy of characterization is investigated. Finally, conclusions are drawn in section 5.

2. Problem formulation

This section briefly reviews dipole source characterization and the design of the ALL system.

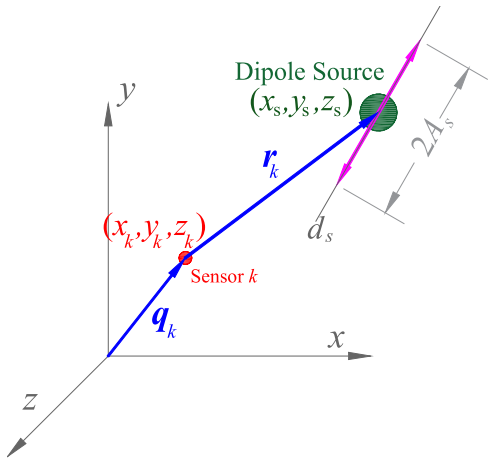

Figure 2. A dipole source located at $[x_s, y_s, z_s]$ vibrates along the line d_s with amplitude of A_s. The disturbance caused by the dipole vibration causes a flow velocity field which can be measured at $q_k = [x_k, y_k, z_k]$ by the sensor k. Vector $\boldsymbol{r}_k$ is the dipole location relative to the sensor k.

2.1. Dipole source characterization

In 3D space, we consider six degrees of freedom for a dipole source (three for locations and three for vibration amplitudes along each direction). The vibration amplitude and frequency are constant which are denoted by A_s and ω_s, respectively (see figure 2). The vibration amplitude A_s is assumed to be unknown. The maximum velocity of the dipole is thus $v_s = A_s \times \omega_s$, the components of which along the coordinate axes are denoted by $\underline{\alpha}_{xs}$, $\underline{\alpha}_{ys}$ and $\underline{\alpha}_{zs}$, respectively. The dipole source can be represented by $\underline{\boldsymbol{\theta}} = [\underline{x}_s, \underline{y}_s, \underline{z}_s, \underline{\alpha}_{xs}, \underline{\alpha}_{.ys}, \underline{\alpha}_{zs}]$, which denotes the true parameters of the source and may be different from those predicted by the ALL.

The flow velocity caused by the dipole's vibration at the kth sensor located at $\boldsymbol{q}_k = [x_k, y_k, z_k]$ is $\boldsymbol{v}(\boldsymbol{q}_k)$, which, in ideal conditions can be computed analytically [24]:

$$\boldsymbol{v}(\boldsymbol{q}_k) = \boldsymbol{F}(\underline{\boldsymbol{\theta}}, \boldsymbol{q}_k),$$
$$\boldsymbol{F}(\underline{\boldsymbol{\theta}}, \boldsymbol{q}_k) = \frac{a_s^3((3\boldsymbol{v}_s \cdot \boldsymbol{r}_k)\boldsymbol{r}_k - \|\boldsymbol{r}_k\|^2 \boldsymbol{v}_s)}{2\|\boldsymbol{r}_k\|^5}. \quad (1)$$

The function $\boldsymbol{F}$ is derived using an analytical flow model and relates the flow field to the dipole parameters. Parameter 'a_s' is the diameter of the dipole, which is typically assumed to be known and $\boldsymbol{r}_k$ is the location of the dipole with respect to the kth sensor. Each sensor is assumed to be able to measure only the magnitude of the local flow velocity along a particular direction $\boldsymbol{n}_k = [n_x, n_y, n_z]_k$, which is the sensing direction of the sensor. The analytical flow velocity component along $\boldsymbol{n}_k$ is:

$$v(\boldsymbol{q}_k) = |\boldsymbol{F} \cdot \boldsymbol{n}_k| = f(\underline{\boldsymbol{\theta}}, \boldsymbol{q}_k, \boldsymbol{n}_k). \quad (2)$$

In ideal situations, this is the value measured and indicated by the sensor. The collective information from the sensors is then used to predict the actual dipole parameters, which is referred to as characterization. Dipole characterization is inherently an inverse problem: For a given set of sensor measurements $(M_k, k = 1, 2, \ldots, N_{\text{sensor}})$, a dipole configuration $(\boldsymbol{\theta})$ is sought such that the corresponding flow field matches the local flow velocity indicated by the sensors. In particular, we define the following objective function:

$$J(\boldsymbol{\theta}) = \frac{\sum_{k=1}^{N_{\text{sensor}}} (M_k - f(\boldsymbol{\theta}, \boldsymbol{q}_k, \boldsymbol{n}_k))^2}{\sum_{k=1}^{N_{\text{sensor}}} (M_k)^2}. \quad (3)$$

By minimizing $J(\boldsymbol{\theta})$, the best candidate dipole source whose flow field matches the given measurements (M_k's) will be found.

In the absence of any uncertainties, the global minimum of the inverse problem $(\boldsymbol{\theta}^*)$ is the actual dipole $(\boldsymbol{\theta}^* = \underline{\boldsymbol{\theta}})$, at which $J(\boldsymbol{\theta}^*) = 0$; however, two types of uncertainty should be considered:

- Sensor uncertainty: The limited precision of the sensors results in an uncertainty in the measured local flow.
- Model uncertainty: The analytical flow model is derived for ideal situations. The actual flow field can be different from the one predicted by (1).

Theoretical models are often derived using some simplifications of the real problem. The accuracy of a theoretical model can be represented as a fraction, for example, ±5%, which means that the model prediction can be 5% different from the actual value. A multiplicative noise can capture this effect, which is employed in this work to incorporate the flow model uncertainty:

$$\underline{M}_k(\underline{\boldsymbol{\theta}}) = \left|f_k(\underline{\boldsymbol{\theta}})\right| \times \exp(\varepsilon_{\text{model}} N(0, 1)), k = 1 \ldots, N_{\text{sensor}}, \quad (4)$$

where $\underline{M}_k$ is the simulated local velocity, $\varepsilon_{\text{model}} \geqslant 0$ denotes the amount of model uncertainty, and $N(0,1)$ is a random number sampled from standard normal distribution.

The sensors typically have a fixed level of precision, independent of the magnitude of the flow velocity. Therefore, similar to previous studies [18, 24], the measurement noise is captured by an additive white Gaussian noise:

$$M_k(\boldsymbol{\theta}) = |\underline{M}_k(\boldsymbol{\theta}) + \varepsilon_{\text{sensor}} N(0, 1)|, \; k = 1, 2, \ldots, N_{\text{sensor}}, \quad (5)$$

where M_k is the sensor measurement and parameter $\varepsilon_{\text{sensor}} \geqslant 0$ denotes the strength of the sensor noise.

These uncertainties are considered to simulate the actual sensor measurements (M_k's), which are different from those predicted by the analytical model. The analytical model, however, is the only available tool to interpret the given sensor measurements in order to solve the inverse problem. Therefore, there are no candidate dipole parameters whose analytical flow field perfectly matches the given measurements, which means $J(\boldsymbol{\theta}^*) > 0$. In general, the predicted dipole parameters obtained by solving the inverse problem are not the actual dipole parameters $(\boldsymbol{\theta}^* \neq \underline{\boldsymbol{\theta}})$. At the same

time, the inverse solver cannot guarantee finding the global minimum ($\boldsymbol{\theta}^*$); in other words, the inverse solver solution ($\widehat{\boldsymbol{\theta}}^* = \left[\widehat{x}_s^*, \widehat{y}_s^*, \widehat{z}_s^*, \widehat{\alpha}_{xs}^*, \widehat{\alpha}_{ys}^*, \widehat{\alpha}_{zs}^*\right]$), might be different from $\boldsymbol{\theta}^*$. The difference between the predicted dipole source by the ALL ($\widehat{\boldsymbol{\theta}}^*$) and $\underline{\boldsymbol{\theta}}$ is the characterization error, which is defined as follows:

$$e = \left\| \left[\frac{\underline{x}_s - \widehat{x}_s^*}{1\text{ cm}}, \frac{\underline{y}_s - \widehat{y}_s^*}{1\text{ cm}}, \frac{\underline{z}_s - \widehat{z}_s^*}{1\text{ cm}} \frac{\underline{\alpha}_{xs} - \widehat{\alpha}_{xs}^*}{1\text{ cm s}^{-1}}, \right.\right.$$
$$\left.\left. \frac{\underline{\alpha}_{ys} - \widehat{\alpha}_{ys}^*}{1\text{ cm s}^{-1}}, \frac{\underline{\alpha}_{zs} - \widehat{\alpha}_{zs}^*}{1\text{ cm s}^{-1}} \right] \right\|. \quad (6)$$

The differences were made dimensionless so that the norm can be computed meaningfully.

2.2. Design problem

To find the best design for an ALL system, we should first specify the design parameters, which depends on the design concept. For example, when six aligned and equally spaced sensors represent the ALL, as used in [24], the only design parameter is the distance between two adjacent sensors. Accordingly, the values of the design parameters are determined using biological inspiration, engineering intuition or numerical optimization. The average characterization error for all possible dipoles can be minimized by proper selection of the design concept and finding the best values for the design parameters.

A reasonable design concept considers a streamlined body, on which the sensors are mounted. This concept has been employed in previous studies [18, 25, 32]. The conformal mapping technique is employed to define the cross-section profile of the cylindrical body and the locations of the sensors on it. For the complex plan $\mathbb{C}$ and a point $\xi \in \mathbb{C}$, ξ is mapped to z with respect to the transformation variable $\lambda \in \mathbb{R}$ using the following transformation [34]:

$$z = \xi + b^2/\xi, \xi = R\exp(\mathrm{i}\beta) - \lambda, b = R - \lambda, \beta \in [-\pi, \pi). \quad (7)$$

This equation defines a disk of radius R, offset along the real axis by $\lambda \in \mathbb{R}$. By choosing b, we can map the disk to a symmetric, streamlined body (see figure 3(a)). Therefore, R specifies the size, $0 < \lambda/R \leqslant 1$ specifies the shape and β_k specifies the location of the kth sensor on the streamlined body. The ALL body turns to a circle and a line segment for $\lambda/R = 1$ and $\lambda/R = 0$, respectively. Other values between these two extremes result in a streamlines body (see figure 3(b)). The 3D ALL body is then generated by extruding this surface along the z-axis. The length of the extrusion determines the thickness of the ALL body (figure 3(c)).

Because of the symmetry in the problem, the sensor locations should be symmetric with respect to the xz-plane. Therefore, only the locations of the sensors on one side of the ALL need to be determined. The sensors are mounted perpendicular to the local curvature of the ALL body (See figure 3). Furthermore, the sensing directions of the sensors ($\boldsymbol{n}_k$'s) are by default tangent to the body [25, 33]. The set of design parameters, $\boldsymbol{X} = [X_1, X_2, \ldots, X_D]$ consists of:

- Size variable: $X_{1\min} \leqslant \mathrm{m} X_1 = R \leqslant X_{1\max}$
- Shape variable: $X_{2\min}\ \mathrm{m}\mathrm{i} X_2 = \lambda/R \leqslant X_{2\max}$.
- Angular position of the first sensor on the fish body: $0\ \mathrm{g}\mathrm{u} X_3 = \beta_1 \leqslant \beta_{\max}$.
- Angular position of the kth sensor relative to the $(k-1)$th sensor: $0\ \mathrm{at} X_k = \beta_{k-2} - \beta_{k-3} \leqslant -\beta_{\max}$, $k = 4,5,\ldots,(N_{\text{sensor}}/2) + 2$,

where N_{sensor} specifies the number of sensors in the ALL. A constraint is defined so that all the independent sensors lie on one size of the symmetry plane.

To evaluate the accuracy of characterization for an arbitrary dipole, we employ the fitness function proposed in our previous studies using 2D setting [25, 33]. The inverse problem is solved for a sample dipole and the characterization error is computed. A characterization score is assigned based on the amount of this error. This process is repeated for N_{dipole} sample dipoles, which calculates N_{dipole} characterization scores. The fitness is then calculated by averaging these scores:

$$g(\boldsymbol{X}) = \frac{1}{N_{\text{dipole}}} \sum_{i=1}^{N_{\text{dipole}}} \exp(-\zeta e_i^2). \quad (8)$$

Here $0 < g(\boldsymbol{X}) \leqslant$ is the fitness of design $\boldsymbol{X}$ which quantifies the accuracy of characterization for an arbitrary dipole configuration. Parameter ζ specifies the score given for a characterization error. A greater ζ assigns a lower credit, resulting in a lower fitness for the corresponding design. The value of $\zeta = 0.1$ is recommended following the parameter study in our previous study [33], which is similarly used in this study. Once a fixed ζ is chosen, a design with a greater fitness is better. The set of N_{dipole} sample dipoles is generated pseudo-randomly using the method proposed in [35, 36]. It improves uniformity of distribution of the sample dipole which provides a better representation of all possible dipoles in the dipole space. If a sample dipole falls inside or very close to the ALL body, a zero score is assigned for that dipole. More dipoles would fall inside if the ALL has a larger body, and thus a smaller ALL body is automatically favored unless a larger body can provide a contribution to characterization accuracy. A larger ALL body leaves less space for possible dipoles, which means less robustness. Without such penalization, the algorithm always converges to a solution with the greatest size, because:

- All sample dipoles will be in a small region of the search space. The optimized design is then specialized for a more specific case in which dipoles are in a smaller region, resulting in a higher fitness.
- A larger ALL provides more diversity in location of the sensors and the gathered information.

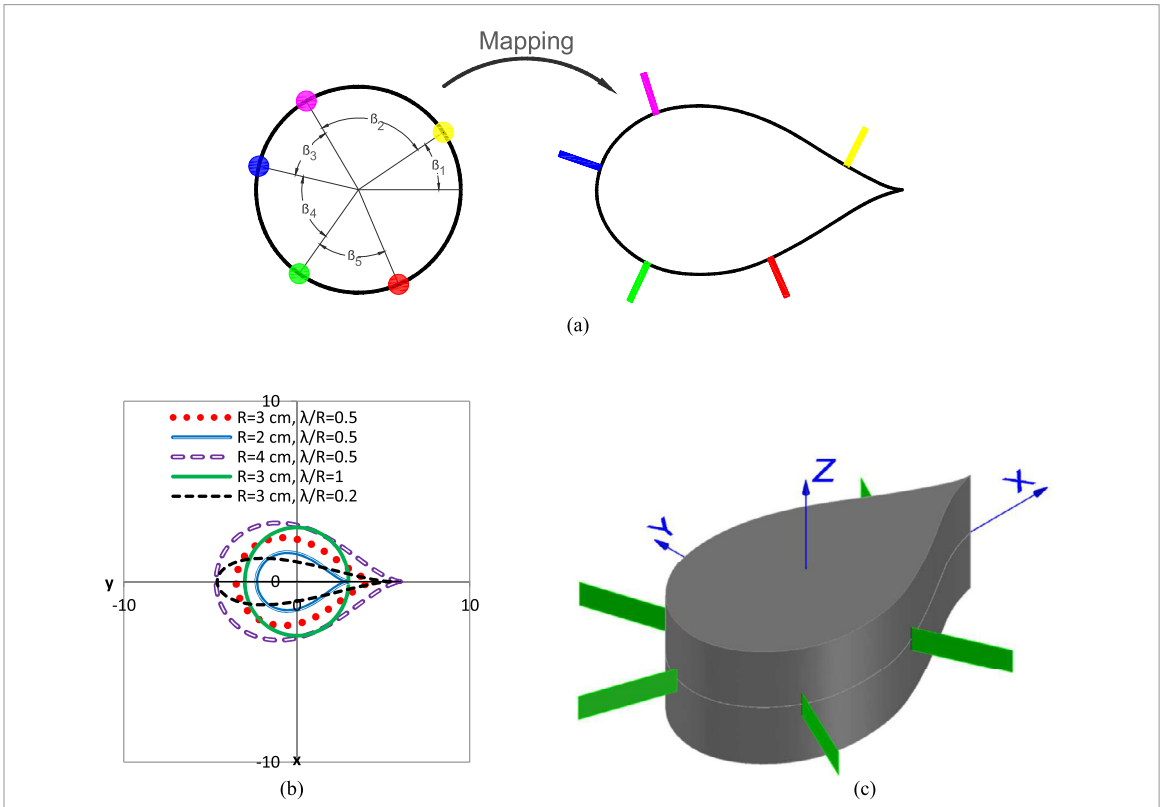

Figure 3. (a) Illustration of the conformal mapping from a disk to a streamline body. The colored lines representing the sensors are perpendicular to the local curvature of the streamlined body. (b) The size and the shape of the streamlined body can be determined by R and λ/R. (c) A typical design in 3D space, where the sensors are perpendicular to the ALL body.

One of the challenges in finding the best design is the randomness of the fitness function, which originates from several types of randomness in the evaluation procedure such as random selection of a finite number of dipoles, and sensor and flow model uncertainties. Independent evaluations of the same design would result in dissimilar calculated finesses, and therefore, algorithms capable of handling noisy fitness functions should be employed for design optimization.

It should be noted that the presence of the ALL body affects the velocity field especially for the regions close to the surface of the ALL body. The employed flow model does not take this effect into account, which results in some error if equation (1) is used to predict the flow field. To the best of our knowledge, there is no simple analytical solution that can capture these fluid-body interactions, while an analytical form is essential for solving the inverse problems considering the number of designs to be evaluated. The error introduced by ignoring the fluid-body interactions, to some extent, is captured by the model uncertainty introduced in section 2.1.

3. Challenges in 3D characterization

The governing equations for the characterization in 3D space, in the vector form, are similar to the 2D case; however, our preliminary investigations using the default design concept, in which sensors and their sensing directions lie in the xy-plane (see figure 3(c)), revealed a drastic decline in characterization accuracy in 3D space in comparison with the 2D space. This indicates there are specific challenges in dipole source characterization in the 3D space. In particular, we speculated that if a dipole lies in certain regions, an ALL cannot provide a reliable characterization. Based on our preliminary analysis and simulations, these challenges can be summarized as follows:

- Equation (1) demonstrates that the velocity components are roughly proportional to $||\boldsymbol{r}||^{-3}$. The dipole can be anywhere in the dipole space and $||\boldsymbol{r}||^2 = (x_s - x_k)^2 + (y_s - y_k)^2 + (z_s - z_k)^2$. For the 2D space, $z_s = z_k = 0$, therefore, the expected value of $||\boldsymbol{r}||$ is smaller. Consequently, on average, the local flow velocity is smaller in 3D than in 2D space. This intensifies the effect of the sensor noise on the measurements, which potentially exacerbates the characterization error.
- The number of the unknown dipole parameters has increased from four to six, which makes the inverse problem harder to solve.
- We discover that the default design concept has blind regions, where a dipole cannot be reliably characterized even if there is no uncertainty. This will be further explored in this section.

For the simulations performed in the rest of this study, the following values for the problem parameters are considered: $X_{1\min} = 0.5$ cm, $X_{1\max} = 4$ cm,

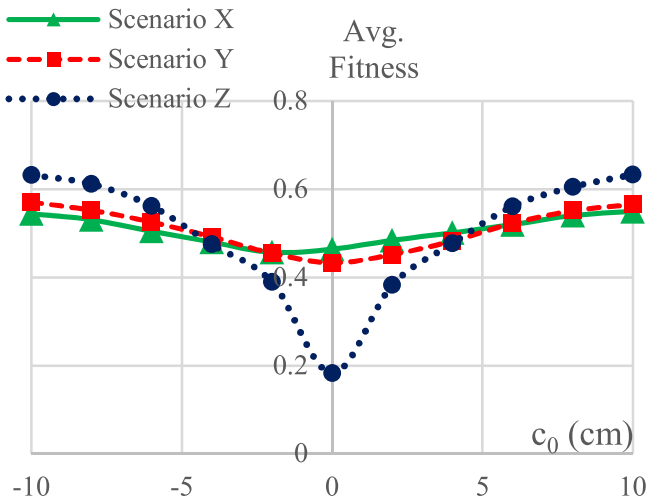

Figure 4. Average fitness in different scenarios as a function of c_0. When all dipoles are on or close to the *xy*-plane (scenario *Z* with $c_0 = 0$), the average fitness is considerably lower. This demonstrates that an ALL cannot characterize a dipole accurately if it lies in this region.

$X_{2\min} = 0.1$, $X_{2\max} = 1$, $\beta_{\max} = 4\pi/N_{\text{sensor}}$. We also assume that the dipole has a known diameter of 1.9 cm. All sample dipoles are in $[-10, 10]$ cm^3. The coordinate-wise components of maximum velocity ($\underline{\alpha}_{xs}$, $\underline{\alpha}_{ys}$ and $\underline{\alpha}_{zs}$) of a sample dipole are randomly selected between -10 cm s^{-c} and 10 cm s^{-1} such that 3 cm s^{-1} $1\text{m}v_s = ||[\underline{\alpha}_{xs}, \underline{\alpha}_{ys}, \underline{\alpha}_{zs}]|| \,|[10\,\text{cm s}^{-1}$. A lower bound on v_s is especially necessary otherwise the local flow velocity will be too small in comparison with the sensor noise. If the sampled dipole violates this constraint, it is discarded and a new dipole is sampled.

3.1. Blind spots

To check possible blind spots for the ALL in the 3D space, we first generate 100 random designs ($N_{\text{sensor}} = 18$, $N_{\text{dipole}} = 256$) and evaluate them in three scenarios:

- Scenario *X*: All dipoles are located at $x = c_0$
- Scenario *Y*: All dipoles are located at $y = c_0$
- Scenario *Z*: All dipoles are located at $z = c_0$

Different values of $c_0 = (-10, -8, -6, \ldots, 10)$ cm are tried one at a time. The values of the dipoles' parameters are selected randomly in the default range, except their *x*, *y*, or *z* location depending on the scenario), which is set to c_0. For each scenario and each value of c_0, we calculate the average fitness of 100 designs ($\overline{f}(c_0)$). At this point, we set $\varepsilon_{\text{model}} = \varepsilon_{\text{sensor}} = 0$ to suppress the possible effects of the uncertainties. Since there are many sample dipoles and the results are averaged over 100 designs, the study can provide a good representation of the average performance for each value of c_0 and each scenario. Figure 4 plots $\overline{f}(c_0)$ in different scenarios. In general, the characterization accuracy is lower if the dipole is closer to the ALL-body; however, this trend is much more drastic for the dipoles close to the *xy*-plane. The average fitness when dipoles are on the plane $z = 0$ is less than one third of the average fitness when they on the plane $z = 10$ cm (compare 0.63 with 0.18), while this difference is at most 33% for dipoles with different *x*-coordinate or *y*-coordinate. This demonstrates that an ALL cannot reliably characterize a dipole if it lies on or close to the *xy*-plane. This region is therefore a blind region for the ALL.

It should be mentioned that this blind region is specific to the problem of the 3D dipole source characterization. In the 2D case, the dipole and its vibration are in the *xy*-plane and this information is provided for the inverse solver. It is a completely different situation in 3D dipole source characterization, since although the dipole may lie on the *xy*-plane, this information is not given to the inverse solver, and therefore it may predict a large *z*-coordinate for the dipole.

3.2. Alternatives for the blind spot challenge

One explanation for the existence of blind regions is that since all sensors are in the *xy* plane and their sensing directions are in *xy*-plane (default design concept), the diversity of the information perceived by the sensors is too limited for a reliable characterization. This explanation is particularly supported by evidence in a previous work [27] that supports advantages of 3D arrangement of sensors for a more robust flow characterization. To test this hypothesis and provide alternatives, we extend the default design concept as follows:

- Offset strategy: Sensors may have offset from the *xy* plane, on which the center plane of the ALL body lies (figure 5(a)). The sensors may have different offsets ($\Delta z_k, k = 1, 2, N_{\text{sensor}}/2$), but all the offset values must be in $[-c_z, c_z]$, where $2c_z$ is equal or smaller than the thickness of the ALL. This strategy leads to the conventional design for $c_z = 0$.
- Angle stagey: The sensors may be mounted such that their normal (sensing direction) lies out of the *xy* plane, but still tangent to the local curvature of the ALL body (figure 5(b)). This out-of-plane

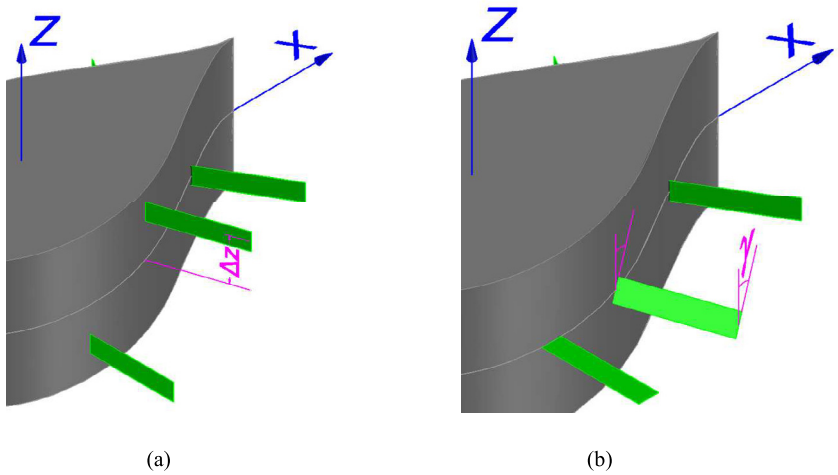

Figure 5. Illustration of the proposed alternative designs for the ALL when (a) offset strategy or (b) angle strategies is used.

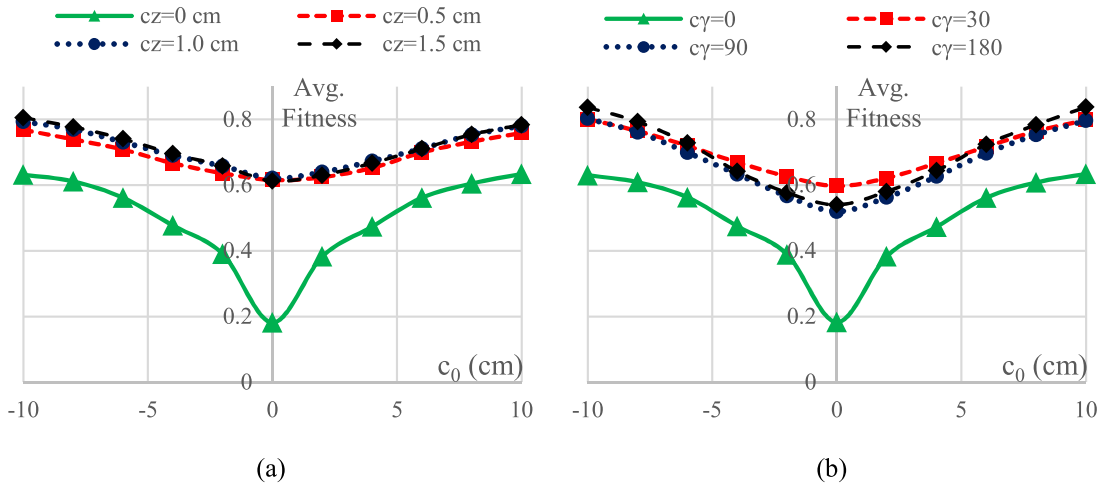

Figure 6. Effect of the proposed design concepts on characterization accuracy when dipoles lie on the *xy*-plane as a function of the (a) maximum allowable offset (c_z) for the offset strategy and (b) maximum allowable rotation angle (c_γ) for the angle strategy. Offsets or rotation angle of individual sensors are not provided in these figures.

sensing direction can be quantified by γ_k, which is the rotation angle of the k-th sensor about its center line. Rotation angles of the sensors ($\gamma_k, k = 1, 2, N_{sensor}/2$) are independent, but all of them must be in $[-c_\gamma, c_\gamma]$. This strategy leads to the conventional design concept for $c_\gamma = 0$.

Both strategies add another design parameter per sensor, and almost double the number of design parameters and presumably increase the prototyping cost. Therefore, only a considerable advantage over the default design concept may justify their suitability.

To investigate and compare these two strategies, 100 random designs are generated using both strategies. The average fitness for different values of c_γ or c_z is calculated while dipoles lie on the *xy*-plane (the blind regions). Figure 6(a) shows this average fitness for the Offset Strategy, when the maximum variation in offsets is limited to $2c_z$. Figure 6(b) shows this average fitness for the Angle Strategy, when the maximum variation in the rotation angles (γ_k's) is limited to $2c_\gamma$. In both cases, providing a slight variation strongly improves the accuracy of characterization for any region. It can particularly address the challenge of blind regions effectively.

One may speculate that the use of multiple smaller ALLs instead of one (with identical overall number of sensors) can improve the dipole source characterization accuracy by providing more flexibility in coordination of the sensors. This flexibility is provided by changing the relative location of the ALLs (δx, δy and δz), which is illustrated in figure 7. For this study, we consider a swarm of three identical ALLs. This means the shape and the size of the ALL bodies are similar, as well as locations and sensing directions of the mounted sensors.

4. Numerical simulation

Similar to our previous method for dipole characterization in the 2D space [33], we employ a bi-level approach to find the optimal design for each design

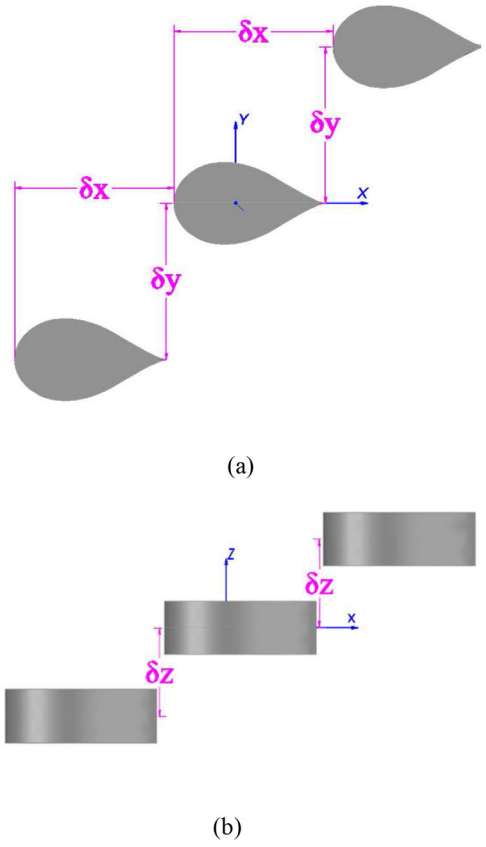

Figure 7. Configuration of multiple ALL (three for this case) can be determined by three design parameters (δx, δy and δz). (a) Top view (view along the z-axis) and (b) front view (view along the y-axis). Sensors are not illustrated.

concept. Considering its efficacy in handling noisy problems [37], covariance matrix adaption evolution strategy (CMA-ES) [38] is employed for the upper level, which optimizes the design parameters ($\boldsymbol{X}$ in (8)). Like all evolutionary algorithms (EAs), CMA-ES is a population-based method, which follows the principles of natural evolution such as selection, recombination and mutations. It is a robust method with minimal assumptions on the problem and can efficiently handle noisy test problems [37], which makes it ideal for our problem.

Since the problem is symmetric, the design parameters are determined such that the final design is symmetric with respect to the xz-plane. The design parameters depend on the selected design concept, which are as follows for different strategies:

- Offset Strategy: Design parameters are the size ($X_1 = R$) and the shape ($X_2 = \lambda/R$) of the ALL body, the relative locations of the sensors on one side of the xz-plane (β_k's, $k = 1, 2, \ldots, N_{\text{sensor}}/2$), and offsets of these sensors from the xy-plane (Δz_k's, $k = 1, 2, \ldots, N_{\text{sensor}}/2$). The overall number of design parameters is thus $N_{\text{sensor}} + 2$, in which N_{sensor} is an even number.
- Angle Strategy: Design parameters are the size ($X_1 = R$) and the shape ($X_2 = \lambda/R$) of the ALL body, relative locations of the sensors on one side of the xz-plane (β_k's, $k = 1, 2, \ldots, N_{\text{sensor}}/2$), and their rotation angles (γ_k's, $k = 1, 2, \ldots, N_{\text{sensor}}/2$). The overall number of design parameters is thus $N_{\text{sensor}} + 2$, in which N_{sensor} is an even number.
- Multiple ALLs: Three ALL systems are identical; therefore, we may design only the middle ALL and determine the relative configuration of these three ALLs. This reduces the number of independent sensors from $N_{\text{sensor}}/2$ to $N_{\text{sensor}}/6$. Design parameters are thus the size ($X_1 = R$) and the shape ($X_2 = \lambda/R$) of the middle ALL body, relative locations of the sensors on one side of the xz-plane for the middle ALL (β_k's, $k = 1, 2, \ldots, N_{\text{sensor}}/6$), the offsets of these sensors from the xy-plane (Δz_k's, $k = 1, 2, \ldots, N_{\text{sensor}}/6$) or the rotation angles of their sensing directions (γ_k's, $k = 1, 2, \ldots, N_{\text{sensor}}/6$) and the relative configuration of these three ALLs with respect to each other, which is determined by three design parameters: δx, δy and δz (see figure 7). The overall number of design parameters is thus $N_{\text{sensor}}/3 + 5$. N_{sensor} must be evenly divisible by 6.

The lower level of our bi-level optimization method solves the inverse problem (minimize $J(\boldsymbol{\theta})$ in equation (3)) using the Newton-Raphson method for N_{dipole} sample dipoles independently, to calculate the fitness of a design according to equation (8). Starting from $N_{\text{dipole}} = 128$, the method doubles N_{dipole} when one-third of the evaluation budget has been used. Similarly, it doubles N_{dipole} again when two-third of the evaluation budget is used. Increasing N_{dipole} reduces the uncertainty in fitness evaluation so that the population may converge to a small region in the search space. At the same time, the population size decreases from 200 to 50 so that the computation cost per iteration ($N_{\text{dipole}} \times PopSize$) remains unchanged. The overall computation budget is measured in terms of *maxJeval*, which is the number of times the error function ($J(\boldsymbol{\theta})$) in the lower loop (equation (3)) is called. For all runs, $maxJeval = 10^9$ is used. Following the performed experiments in [25], the sensor noise was set to $\varepsilon_{\text{sensor}} = 0.0015$ cm s^{-1}. The value of $\varepsilon_{\text{sensor}}$ was set to 0.01. The ideal case (no uncertainty) is also investigated for comparison. $a_s = 1.9$ cm is known for all sample dipoles.

4.1. Optimization results

This subsection examines the advantages of the proposed design concepts compared to the default concept. Each design concept is optimized when different values for c_z or c_γ, varying from zero to a reasonable upper value, are tried. This upper value is 90° for the angle strategy and half of the thickness of the ALL body for the offset strategy, which is assumed to be 1.5 cm in here. Testing different values c_z or c_γ illuminates contribution of extra variation in the sensing direction or z-coordinates of the sensors to the characterization accuracy. For both strategies, $c_z = 0$ or $c_\gamma = 0$ automatically reduces the strategy to the default design concept, where sensors and their sensing

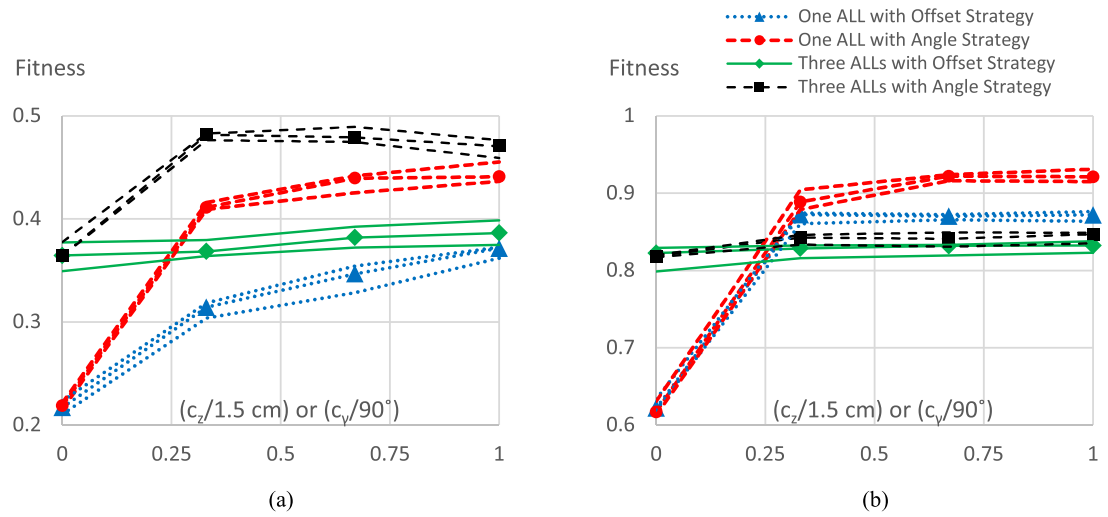

Figure 8. Median (lines with markers) and the lowest and the highest (lines without markers) fitness when different number of ALLs (one or three) and different strategies (angle or offset) are used. The horizontal axis is the maximum allowable variation in the offset (c_z) or the angle (c_γ) strategy for (a) the realistic case (with uncertainties) and (b) ideal case (no uncertainties).

directions are in the xy-plane. $N_{\text{sensor}} = 18$ is considered at this stage. Overall:

- Eight different values for the maximum variation in the sensors' offsets ($c_z = 0, 0.5$ cm, 1 cm and 1.5 cm) or rotation angles ($c_\gamma = 0°, 30°, 60°$ and 90°) are investigated.
- Both cases of one ALL and three ALLs are investigated for both the angle and the offset strategies (two options)
- Both the ideal case and the realistic case are considered (two options).

Therefore, $8 \times 2 \times 2 = 32$ combinations are investigated. Five independent optimization runs are performed for every combination. The final best solutions for each run are reevaluated using a large N_{dipole} ($N_{\text{dipole}} = 10\,240$) to provide a substantially more accurate estimation of the true fitness, resulting in five best values for each combination. The median of these five values represents the fitness of the optimized solution for that combination. Aside from the fitness value, the median of the size parameter ($X_1 = R$) and the shape parameter ($X_2 = \lambda/R$) in these five design represent the size and the shape of the optimized design for the corresponding combination.

Figure 8 illustrates the median, lowest and highest reevaluated fitness of the five optimized designs for each combination. The same statistics for the size and shape values are plotted in figure 9. Figure 10 plots the rotation angles (β_k's) and positions of individual sensors (γ_k's) for a specific combination (one ALL in realistic case, $c_\gamma = 90°$). The best designs for single ALL and multiple ALLs using the angle strategy in realistic case are illustrated in figure 11. These figures reveal that:

- Figure 8 demonstrates that for each combination, fitness values of the final solutions from independent runs are close. This is a checkpoint for significance of the optimization results and the importance of the design concept.
- For both the ideal case (figure 8(b)) and the realistic case (figure 8(a)) with only one ALL, the fitness of the optimized designs dramatically improves if the sensing direction or the z-coordinates of the sensors can be changed. Using multiple ALLs has a similar effect. When the uncertainties are considered (figure 8(a)), multiple ALLs with varying sensing directions results in the maximum accuracy, while the offset strategy does not provide any additional advantage. This is expected, since multiple ALLs already provide diversity in the z-coordinates of the sensors. For the case with no uncertainty, using multiple ALLs is a disadvantage (figure 8(b)).
- For both the ideal case (figure 8(b)) and the realistic case (figure 8(a)), the angle strategy provides a significant contribution when c_γ increases from 0° to 30°; however, greater values do not provide considerable extra contributions. Extra flexibility in c_z provides considerable contribution only in the case of one ALL in uncertain environment (figure 8(a)). For the ideal case (no uncertainty), diversity of measurements loses its importance and for the case with multiple ALL, extra diversity can be provided by controlling the relative locations of ALLs.
- Figures 9(a) and (b) demonstrate that the sizes of the final designs depend on not only the uncertainty amount, but also possible variation in the sensing direction or z-coordinates of the sensors as well as the use of multiple ALLs. As a general trend, the optimized ALL is smaller when multiple ALLs are used or uncertainties are excluded (compare figures 9(a) with (b)). This observation is expected: When there is no uncertainty, diversity of the sensor data loses

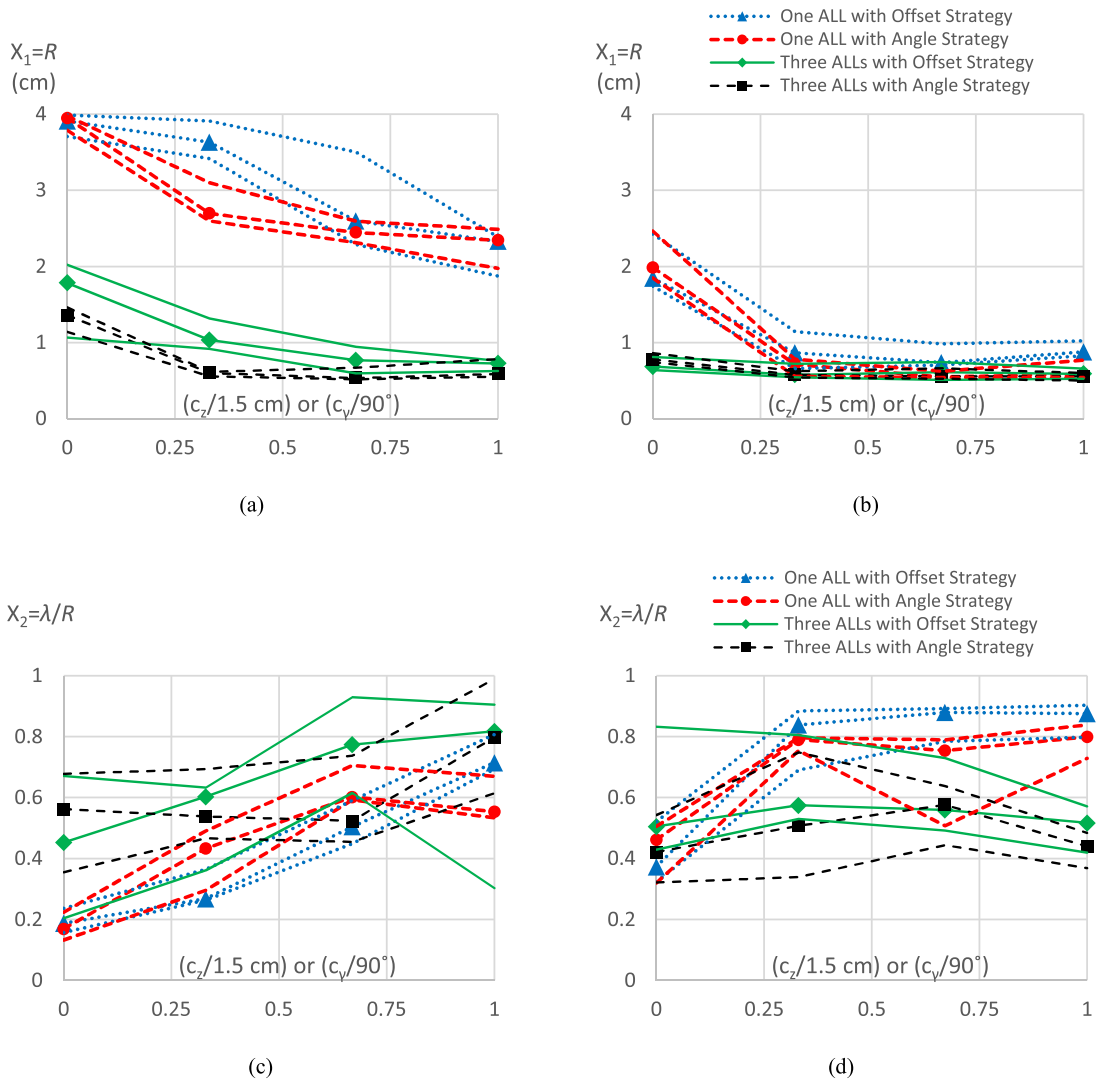

Figure 9. Median (lines with markers) and the lowest and the highest (lines without markers) values of the size ($X_1 = R$ cm) and shape ($X_2 = \lambda/R$) of the final solutions of five independent runs with different strategies in the realistic case (left) and the ideal case (right). Plots are provided for different strategies (one ALL or three ALLs, Angle or Offset) with different values for maximum variation of the offset or rotation angle.

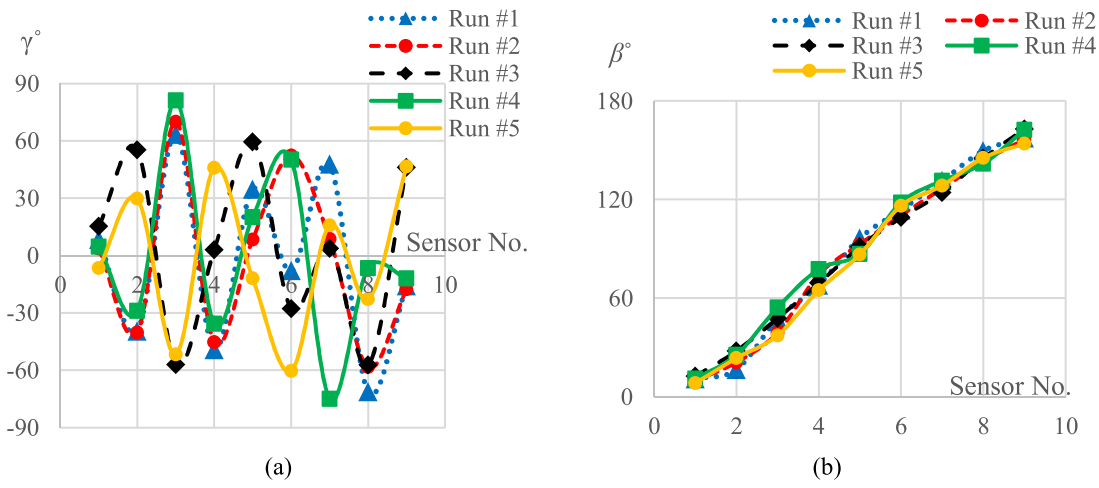

Figure 10. Optimized solutions from five independent runs in realistic case ($N_{\text{sensor}} = 18, c_\gamma = 90°$). Sensors are numbered sequentially from tail to tip. (a) Rotation angles of the sensors (γ_k's) in degree and (b) positions of the sensors (β_k's) in degree.

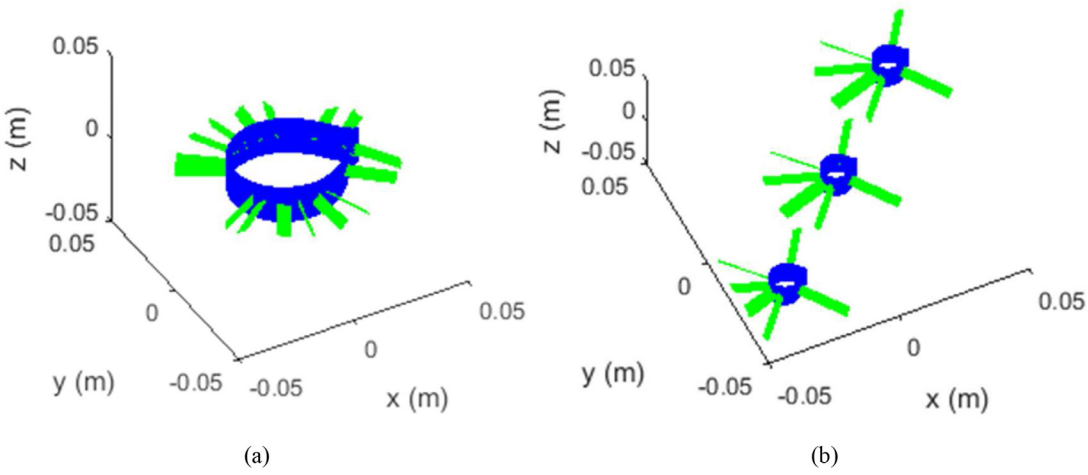

Figure 11. Best solutions in the angle strategy in uncertain conditions for $N_{\text{sensor}} = 18$. (a) One ALL and (b) three identical ALLs ($\delta x = 3.2$ cm, $\delta y = 2.7$ cm, $\delta z = 3.1$ cm).

its importance. The algorithm reduces the size of the ALL to minimize the number of sample dipoles that are inside or too close to the body, for which the design receives zero scores. Multiple ALL systems provide diversity by controlling the distance between the ALLs, and therefore a large body is not needed anymore. Increasing c_γ or c_z also favors smaller ALLs (figures 9(a) and (b)). A detectable similarity among the size of the final solutions from independent runs is observed, which confirms the efficacy of the optimization and significance of the design model.

- Unlike the size, shapes of the optimized solutions from independent runs are not similar (figures 9(c) and (d)). This implies that the shape is not so sensitive as size and there is a comparatively wide range for the near-optimal shape parameter. Since fitness of these solutions is close, the selection operator may be misguided by the noise in evaluation of the fitness. It can still be observed that increasing c_γ or c_z results in a more circular shape when one ALL is employed. Using a significantly higher N_{dipole} for optimization reduced the noise in design evaluation and can moderate this negative effect, and thus may result in a narrower range for the shape values. It comes at the cost of significantly higher computation time.
- Although rotation angles in the optimized designs from five independent runs are not similar (figure 10(a)), there are certain common properties among these optimized designs. First, for all the optimized designs, the rotation angles are distributed over a large range in $[-90°, 90°]$. Second, for each optimized design, a sinusoidal distribution of rotation angles is observed. This implies that there is no optimal rotation angle for a specific sensor. The variation in rotation angle of the sensors in the design and dissimilarity of the rotation angles of two adjacent sensors are of prominent importance. Unlike the rotation angles, the positions of the sensors (figure 10(b)) in the optimized designs are quite similar. This similarity is a checkpoint for efficacy of the optimization results. Besides, it may confirm that unlike the sensor rotation angles, there is almost a unique set of optimal sensor positions.
- Figure 11 demonstrates that when three ALLs are used, the individual ALLs are much smaller than the case when a single ALL is used. For the former case, δx, δy and δz are non-zero. This allows for another type of diversity in locations of the sensors, although it reduces the diversity in the sensing angles and x and y coordinates of the sensors.

4.2. Bi-objective optimization

Since the simulated uncertainties are unbiased and uncorrelated, it is predicted that increasing the number of sensors improves the characterization accuracy, as it was demonstrated in our earlier work in the 2D space [33]; however, more sensors increase the fabrication cost. Decision on N_{sensor} can be guided by observing the trade-off between N_{sensor} and the characterization accuracy. This section investigates this trade-off by performing optimization for different values of N_{sensor}. $c_\gamma = 90°$ and $c_z = 1$ cm for the angle and the offset strategies are considered and both single and multiple (three) ALL systems are tested. The median, the lowest and the highest fitness of the final solutions for each case is presented in figure 12:

- Figure 12(b) demonstrates that using multiple ALLs is advantageous for the case with no uncertainties. The angle strategy is more beneficial than the offset strategy. In particular, one ALL with the angle strategy is the best choice, except for a very low number of sensors. Increasing the number of sensors improves the fitness up to $N_{\text{sensor}} = 18$; however, no considerable improvement can be observed after that.

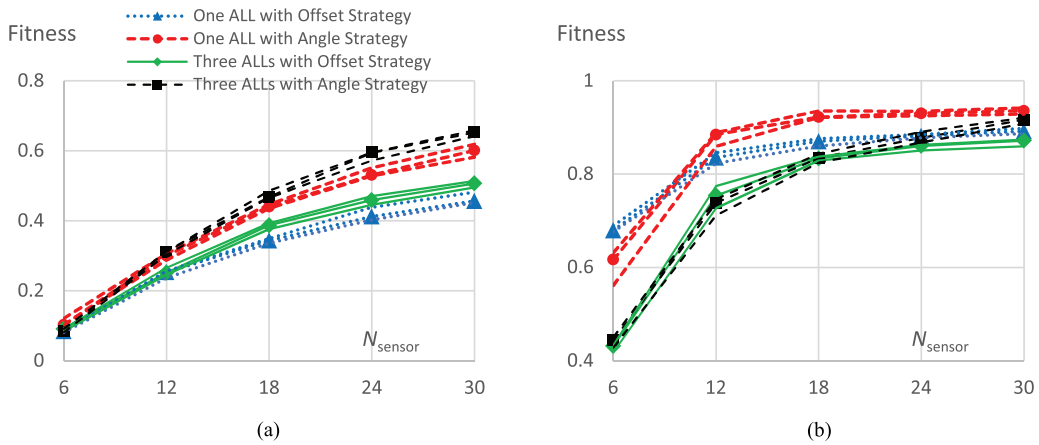

Figure 12. Trade-off between the number of sensors and the fitness for the cases with one or three ALL using angle or offset strategies for the case (a) with uncertainties and (b) without uncertainties. For each case, the lines with markers represent the median values and the lines with no markers represent the highest and the lowest values in five independent runs.

- Figure 12(a) demonstrates that the angle strategy should be preferred over the offset strategy for the realistic case; however, unlike the ideal case, using multiple ALLs can provide a considerable advantage. Furthermore, extra sensors can continually improve the fitness in the realistic case, at least up to $N_{sensor} = 30$.

5. Summary and conclusions

This study has concentrated on optimum design of the ALL system in the 3D space to maximize the average accuracy of characterization for all possible dipole sources with six degrees of freedom. While the earlier research in the 2D space was a good starting point for research on underwater object detection, the real environment is 3D. Extending the same methodology to the 3D-space faces some new challenge which reduces the characterization accuracy. We have demonstrated that the use of linear or even in-plane arrangement for the sensor locations and their sensing directions (the default design concept) has resulted in a failure in dipole characterization if the dipole source is in the plane of the ALL. This was unexpected because such dipoles, on average, are closer to the sensors, and thus generate a stronger flow at the sensors. We have proposed two distinct alternative design concepts to overcome the challenge of blind regions: The alternative design concepts has allowed the sensors to lie out of the ALL-body plane (offset strategy) or have different out-of-plane sensing directions (angle strategy). Our numerical simulations have demonstrated that these alternatives can not only overcome the challenge of the blind regions, but also improve characterization accuracy for a dipole source in any other region. The use of multiple but identical ALL systems with the same number of sensors has been also investigated in conjunction with both aforementioned design concepts. This can be regarded as a swarm of ALL systems and may simulate collective knowledge of a fish school in nature.

For each design concept, optimization has been performed with a fixed number of sensors while the model and sensor uncertainties are simulated (realistic case) or disregarded (ideal case). The optimized designs of the proposed design concepts have appeared to be superior to the designs obtained from the default concept. A comparison of the optimized designs has revealed that the uncertainties can, not only reduce characterization accuracy, but also affect optimal selection of the design concept and the design parameters. To address the practical needs, consideration and simulation of these uncertainties have been found to be critically important. For example, the angle strategy has turned out to be a better choice, whereas using multiple similar ALLs was advantageous only for the realistic case. The shape and the size of the optimized ALL body has also turned out to be dependent on the employed design strategy and presence of uncertainties. A trade-off between the number of sensors and the characterization accuracy has revealed that higher characterization accuracy in uncertain conditions can be obtained by increasing the number of sensors. For the ideal case, more sensors have shown to improve the accuracy up to 18 sensors, and after that no considerable contribution of extra sensors could be detected. Such analyses facilitate making decision on the number of sensors to maximize accuracy of the characterization for a fixed cost.

A design problem has many diverse solutions. It is difficult to hit upon an optimum by chance or by creating a solution from past experience. Optimization algorithms can help provide near- optimum solutions in a systematic manner; however, any expert knowledge about a problem can aid an optimization algorithm's performance, if the chosen algorithm can utilize the supplied knowledge appropriately. In this paper, we have considered an ALL design problem and demonstrated that providing information through an offset strategy and angle strategy may result in a significant

improvement in the dipole characterization accuracy. The promising results of multiple ALLs motivate further research on swarming robotic fish. Although the special case for three ALLs was studied here, the number of ALLs can be optimized as well. Finally, we highlight here that the findings in this study are obtained for the streamlined body shape only. As a future study, we plan to examine whether the findings of this study extend to other 3D shapes for more pragmatic ALL system, such as having ellipsoidal or cylindrical shapes.

Acknowledgment

Computational work in support of this research was performed at Michigan State University's High Performance Computing (HPCC) Facility. This material was based in part upon work supported by the National Science Foundation under Cooperative Agreement No. DBI-0939454 and by the Office of Naval Research (N000141210149, N000141502246). Any opinions, findings, and conclusions or recommendations expressed in this material are those of the author(s) and do not necessarily reflect the views of the National Science Foundation or the Office of Naval Research.

References

[1] Bleckmann H 1994 *Reception of Hydrodynamic Stimuli in Aquatic and Semiaquatic Animals* (Stuttgart: Gustav Fischer Verlag)
[2] Liao J C 2006 The role of the lateral line and vision on body kinematics and hydrodynamic preference of rainbow trout in turbulent flow *J. Exp. Biol.* **209** 4077–90
[3] Pitcher T J, Partridge B L and Wardle C S 1976 A blind fish can school *Science* **194** 963–5
[4] Bleckmann H, Przybilla A, Klein A, Schmitz A, Kunze S and Brücker C 2012 Station holding of trout: behavior, physiology and hydrodynamics *Nature-Inspired Fluid Mechanics* (Berlin: Springer) pp 161–77
[5] Montgomery J C, Baker C F and Carton A G 1997 The lateral line can mediate rheotaxis in fish *Nature* **389** 960–3
[6] Stewart W J, Nair A, Jiang H and McHenry M J 2014 Prey fish escape by sensing the bow wave of a predator *J. Exp. Biol.* **217** 4328–36
[7] Von Campenhausen C, Riess I and Weissert R 1981 Detection of stationary objects by the blind cave fish anoptichthys jordani (Characidae) *J. Comp. Physiol.* **143** 369–74
[8] Engelmann J, Hanke W, Mogdans J and Bleckmann H 2000 Hydrodynamic stimuli and the fish lateral line *Nature* **408** 51–2
[9] Bleckmann H 2008 Peripheral and central processing of lateral line information *J. Comp. Physiol.* A **194** 145–58
[10] Bruun H H 1995 *Hot-Wire Anemometry: Principles and Signal Analysis* (Oxford: Oxford University Press)
[11] Yang Y, Chen J, Engel J, Pandya S, Chen N, Tucker C, Coombs S, Jones D L and Liu C 2006 Distant touch hydrodynamic imaging with an artificial lateral line *Proc. Natl Acad. Sci.* **103** 18891–5
[12] Rizzi F, Qualtieri A, Chambers L D, Epifani G, Megill W M and De Vittorio M 2014 Stress-driven artificial hair cell for flow sensing *Flow Sensing in Air and Water* (Berlin: Springer) pp 499–519
[13] Kottapalli A G P, Asadnia M, Miao J and Triantafyllou M 2014 Touch at a distance sensing: lateral-line inspired MEMS flow sensors *Bioinspir. Biomim.* **9** 046011
[14] Lei H, Li W and Tan X 2012 Microfabrication of IPMC cilia for bio-inspired flow sensing *Proc. SPIE* **8340** A83401
[15] DeVries L, Lagor F, Lei H, Tan X and Paley D 2015 Distributed flow estimation and closed-Loop control of an underwater vehicle with a multi-modal artificial lateral line *Bioinspir. Biomim.* **10** 025002
[16] Hassan E S 1993 Mathematical description of the stimuli to the lateral line system of fish derived from a three-dimensional flow field analysis *Biol. Cybern.* **66** 443–52
[17] Ren Z and Mohseni K 2012 A model of the lateral line of fish for vortex sensing *Bioinspir. Biomim.* **7** 036016
[18] DeVries L and Paley D A 2013 Observability-based optimization for flow sensing and control of an underwater vehicle in a uniform flowfield *Proc. of American Control Conf. (Washington, DC)*
[19] Windsor S P, Norris S E, Cameron S M, Mallinson G D and Montgomery J C 2010 The flow fields involved in hydrodynamic imaging by blind Mexican cave fish (Astyanax fasciatus). Part I: open water and heading towards a wall *J. Exp. Biol.* **213** 3819–31
[20] Windsor S P, Norris S E, Cameron S M, Mallinson G D and Montgomery J C 2010 The flow fields involved in hydrodynamic imaging by blind Mexican cave fish (Astyanax fasciatus). Part II: gliding parallel to a wall *J. Exp. Biol.* **213** 3832–42
[21] Akanyeti O, Venturelli R, Visentin F, Chambers L, Megill W M and Fiorini P 2011 What information do Karman streets offer to flow sensing *Bioinspir. Biomim.* **6** 036001
[22] Ristroph L, Liao J C and Zhang J 2015 Lateral line layout correlates with the differential hydrodynamic pressure on swimming fish *Phys. Rev. Lett.* **114** 018102
[23] Akanyeti O, Chambers L D, Ježov J, Brown J, Venturelli R, Kruusmaa M, Megill W M and Fiorini P 2013 Self-motion effects on hydrodynamic pressure sensing: part I. Forward–backward motion *Bioinspir. Biomim.* **8** 026001
[24] Abdulsadda A T and Tan X 2013 Nonlinear estimation-based dipole source localization for artificial lateral line systems *Bioinspir. Biomim.* **8** 026005
[25] Ahrari A, Lei H, Sharif M A, Deb K and Tan X 2015 Design optimization of artificial lateral Line system under uncertain conditions *Proc. of IEEE Congress on Evolutionary Computation (CEC 2015) (Sendai, Japan)* (IEEE) pp 1807–14
[26] Dagamseh A M K, Lammerink T S J, Kolster M L, Bruinink C M, Wiegerink R J and Krijnen G J M 2010 Dipole-source localization using biomimetic flow-sensor arrays positioned as lateral-line system *Sensors Actuators* A **162** 355–60
[27] Chambers L D *et al* 2014 A fish perspective: detecting flow features while moving using an artificial lateral line in steady and unsteady flow *J. R. Soc. Interface* **11** 20140467
[28] Abdulsadda A T and Tan X 2013 Underwater tracking of a moving dipole source using an artificial lateral line: algorithm and experimental validation with ionic polymer–metal composite flow sensors *Smart Mater. Struct.* **22** 045010
[29] Venturelli R *et al* 2012 Hydrodynamic pressure sensing with an artificial lateral line in steady and unsteady flows *Bioinspir. Biomim.* **7** 036004
[30] Abdulsadda A T and Tan X 2012 Underwater tracking and size-estimation of a moving object using an IPMC artificial lateral line *Proc. of ASME 2012 Conf. on Smart Materials, Adaptive Structures and Intelligent Systems* pp 657–65
[31] Abels C, Qualtieri A, Vittorio M D, Megill W M and Rizzi F 2015 A bio-inspired real-time capable artificial lateral line system for freestream flow measurements *Bioinspir. Biomim.* **11** 035006
[32] Yang Y, Nguyen N, Chen N, Lockwood M, Tucker C, Hu H, Bleckmann H, Liu C and Jones D L 2010 Artificial lateral line with biomimetic neuromasts to emulate fish sensing *Bioinspir. Biomim.* **5** 016001
[33] Ahrari A, Lei H, Sharif M A, Deb K and Tan X 2017 Design optimization of an artificial lateral line system incorporating flow and sensor uncertainties *Eng. Optim.* **49** 328–44
[34] Panton R L 1984 *Incompressible Flow* (New York: Wiley)
[35] Ahrari A and Atai A A 2010 Grenade explosion method—a novel tool for optimization of multimodal functions *Appl. Soft Comput.* **10** 1132–40

[36] Ahrari A, Shariat-Panahi M and Atai A A 2009 GEM: a novel evolutionary optimization method with improved neighborhood search *Appl. Math. Comput.* **210** 376–86
[37] Hansen N 2009 Benchmarking a BI-population CMA-ES on the BBOB-2009 noisy testbed *Proc. of the 11th Annual Conf. Companion on Genetic and Evolutionary Computation Conf.: Late Breaking Papers*
[38] Hansen N and Ostermeier A 2001 Completely derandomized self-adaptation in evolution strategies *Evol. Comput.* **9** 159–95